

Datacube Parametrization-Based Model for Rough Surface Polarimetric Bistatic Scattering

Xueyang Duan* and Mark Haynes

Abstract—A datacube parametrization-based model for bistatic scattering coefficient estimation, and pattern reconstruction is presented in this work for electromagnetic wave scattering from rough surfaces with low to high subsurface dielectric constants. A datacube of bistatic scattering coefficients is simulated using the Stabilized Extended Boundary Condition Method (SEBCM). The polarization-combined bistatic scattering patterns of the datacube are fit with elliptical (or circular) contours that are parameterized across magnitude level, center location, and major axis length in normalized wavenumber space. These parameters depend on the surface roughness, dielectric contrast, as well as the angle of wave incidence. The polarimetric bistatic scattering patterns can be reconstructed through fast interpolation over the contours and projection onto the polarization unit vectors. Good agreement is achieved between the reconstructed bistatic scattering patterns compared with the original ones in the input datacube. Though not physics-based, this datacube parametrization-based model allows quick estimation and construction of the polarimetric bistatic scattering coefficients and patterns. The model development approach can also be adopted to parametrize datacubes from simulations with other configurations or targets, e.g., surface with different correlation functions, multilayer surfaces, surface covered with vegetation, etc..

1. INTRODUCTION

In this work, we present a method for efficiently predicting the bistatic polarimetric scattering coefficients for random rough surface over a range of surface roughnesses, dielectric properties, and incident and scattering directions. This method is based on a datacube-derived analytical model of bistatic scattering coefficients. The model itself, or its extrapolation, can be applied to predict bistatic scattering coefficients in forward modeling and performance evaluation of bistatic or multistatic radar remote sensing of natural targets. The datacube approach here is general enough that it can be expanded or adopted to build similar bistatic scattering models from datacubes simulated with other configurations of interest.

The need for fast generation of bistatic polarimetric scattering coefficients and patterns is motivated by the problem of simulating radar scattering from electrically-large surfaces which exhibit both large-scale and small-scale roughness. For electrically-large surfaces, flat facets can be used to capture the scattering effects of large-scale roughness and/or topography and have been used for a number of applications including general synthetic aperture radar [1], low-frequency radar sounding and multi-layer simulation [2, 3], scattering from ocean surfaces and altimetry [4–6], and moving targets [7]. For homogenous scenes, facet orientation and size can be used and easily augmented with basic backscatter σ_o curves to simulate incoherent scattering due to small scale roughness. However, for inhomogeneous scenes, or more complicated cases of bistatic or multi-layer transmission simulations, storing and

Received 8 December 2020, Accepted 11 January 2021, Scheduled 18 January 2021

* Corresponding author: Xueyang Duan (Xueyang.Duan@jpl.nasa.gov).

The authors are with the Jet Propulsion Laboratory, California Institute of Technology, 4800 Oak Grove Drive, Pasadena, CA 91109, USA.

sampling the full bistatic scattering matrix can be computationally expensive. In addition, we desire to reproduce the Rayleigh scattering statistics of the incoherent scattering component. The problem we focus on in this work is not the large-scale performance of aggregating facet echoes, but a way to quickly and efficiently predict statistically accurate bistatic polarimetric scattering coefficients, in order that they can be more effectively used with general radar simulators.

To-date, many computational electromagnetic models are capable of calculating bistatic scattering coefficients from rough surfaces exist, including both analytical and numerical methods. The analytical solutions are widely used in bistatic scattering studies, including the Kirchhoff and perturbation approximation [8–11], the small perturbation method [12, 13], and the small slope approximation [14]. These analytical methods can quickly calculate scattering coefficients but are valid only for relatively smooth surfaces. On the other hand, fully numerical solutions, including the method of moments [15–17], the integrated equation method (IEM) [18], and the advanced IEM [19], are able to compute bistatic scattering coefficients for any roughness, but at a price of much greater computational complexity. In this work, we use the stabilized extended boundary condition method (SEBCM) [20] to simulate the datacube of bistatic scattering coefficients in all directions as a function of surface roughness and dielectric properties. This method has much higher computational efficiency than the fully numerical methods, and gives accurate full wave solutions to the vector scattered fields from surfaces with large roughnesses ($k_0h < 1.0$). In particular, this method computes the rough surface scattering from all bistatic combinations at once, which makes this method a preferred one for bistatic scattering study. A Monte Carlo process has been carried out to simulate a hundred surface realizations for each roughness-dielectric configuration to create the datacube of bistatic scattering coefficients.

The goal is to parametrize the simulated datacube so that for any given combination of surface roughness and subsurface dielectric, we can quickly obtain the bistatic scattering coefficients at all incident and scattered directions of interest, for both magnitude and phase. As the phase of the scattering coefficient is a uniformly distributed random variable, our parametrization is focused on the scattering coefficient magnitude, which is a random variable with Rayleigh distribution. The scale factor of the Rayleigh distribution can be uniquely determined by the mean of the scattering coefficient magnitudes from the Monte Carlo process. In this work, we have concentrated on building a model for bistatic scattering when the incident wave reflects from a medium with low dielectric permittivity to a medium with high dielectric permittivity.

After combining the two scattering components projected onto H - and V -polarizations, our parametrization is built on the observation that the average bistatic scattering patterns can be represented reasonably well by a group of elliptical contours in the normalized wavenumber space. These elliptical contours can further be approximated by circular contours. The contours can be described by their magnitude levels, center locations, and major axis lengths. These parameters depend on the surface roughness properties, dielectric contrast, and angle of wave incidence. By parametrizing these dependencies and fitting for the parameters as a function of surface properties and direction of wave incidence, the polarimetric bistatic scattering patterns can then be reconstructed through interpolation over the contours and projection onto the polarization unit vectors.

Bistatic scattering patterns reconstructed from the datacube parametrization using this method show good agreement with the simulated patterns over a majority of surface configurations. Reconstruction RMSEs have been evaluated and are presented with respect to roughness, dielectric contrast, and angle of incidence, which help to inform the reconstruction error when using the model for bistatic coefficient estimation for the cases of interest. On average, we found that the reconstruction RMSE increases as the angle of incidence gets closer to the grazing angle. RMSE is also larger in the reconstructed VV patterns than those in the HH and the HV patterns, which have averaged RMSE ranging from 2 to 3.5 dB. Though not physics-based, the datacube parametrization-based model presented here allows quick reconstruction of the polarimetric bistatic scattering coefficients. This approach can also be applied to parametrize bistatic scattering datacubes from simulations of other configurations or targets, e.g., surfaces with different correlation functions, multilayer media, surfaces covered with vegetation, etc.

The paper is organized as follows: Section 2 describes the approach of datacube simulation and parametrization; Section 3 presents the pattern reconstruction process and results, as well as RMSE evaluation; finally, Section 4 concludes this paper with further discussion and future work.

2. DATACUBE SIMULATION AND PARAMETRIZATION APPROACH

2.1. Datacube Simulation

The Stabilized Extended Boundary Condition Method (SEBCM) [20] is used in this work to simulate the bistatic scattering coefficient datacubes. For each rough surface realization, this model is capable of computing the bistatic polarimetric scattering matrix $S_{pq}^{mn}(\theta_s, \phi_s; \theta_i, \phi_i)$ as a function of the above- and the below-surface dielectric constants, and the surface roughness described by the root-mean-square height h and the surface correlation length l . Let the numbers ‘1’ and ‘2’ note the media above and below the surface, respectively, the subscript m ($m = 1$ or 2) notes the medium of observation, and the subscript n ($n = 1$ or 2) notes the medium of incidence. The superscripts p and q ($p, q = \text{H or V}$) note the polarization of the scattered and the incident wave, respectively. The exponential correlation function with its spectral density shown in Eq. (1) and Eq. (2) is used to generate random rough surfaces in this work. The exponential correlation appears to better match experimental data [21] than Gaussian correlation functions. Distances in the spatial domain and the wavenumber domain are noted by \bar{r}_\perp and \bar{k}_\perp , respectively.

$$C(\bar{r}_\perp) = \exp\left(-\frac{|\bar{r}_\perp|}{l}\right) \tag{1}$$

$$W(\bar{k}_\perp) = \frac{h^2 l^2}{2\pi (1 + \bar{k}_\perp^2 l^2)^{\frac{3}{2}}} \tag{2}$$

The surface parameters, their ranges, and step sizes that are simulated and therefore sample the datacube are listed in Table 1. Note that although the bistatic scattering matrix contains incidence over all azimuth directions (i.e., ϕ_i from 0 to 2π), we only need to analyze the bistatic scattering patterns excited by the incidence from one azimuth direction ($\phi_i = 0$ in this work), because the correlation function is isotropic. The surface correlation length l is fixed to be 10 times of the surface RMS height h , which is the typical value used in modeling scattering from ground. For each surface configuration, a Monte Carlo process of 100 surface realizations was computed using the JPL High Performance Computing (HPC) resource. Roughly 165,000 CPU hours were required for the datacube generation.

Table 1. Value range of simulation parameters.

parameters	start value	step value	stop value
RMS height in terms of wavelength in free space h/λ_0	0.01	0.01	0.1
real part of dielectric constant in medium 1 $\epsilon_r^{(0)}$	1	1	10
imaginary part of dielectric constant in medium 1 $\epsilon_i^{(0)}$	0.01	0.01	0.1
real part of dielectric constant in medium 2 $\epsilon_r^{(1)}$	1	1	10
imaginary part of dielectric constant in medium 2 $\epsilon_i^{(1)}$	0.01	0.01	0.1

Figure 1 shows an example of the averaged bistatic scattering patterns from one surface configuration (rms height of $0.7 \cdot \lambda_0$ and lossless medium with $\epsilon_r^{(0)} = 1$ and $\epsilon_r^{(1)} = 3$) for one angle of incidence. Figure 2 shows the magnitude and phase statistics for one scattering direction. As expected, among the 100 realizations from the Monte Carlo process, the magnitude and the phase of the scattering coefficients at a given scattering direction follow a Rayleigh distribution and uniform distribution, respectively. Therefore, given the mean of the bistatic scattering pattern, a realization of the magnitude of the scattering coefficient in any direction can be obtained as a Rayleigh random variable. This implies that, in effect, we are treating the total power as being composed of strictly incoherent energy. The analytical model to reconstruct the bistatic scattering pattern in the upper medium above the surface, i.e., S_{11} , is developed below.

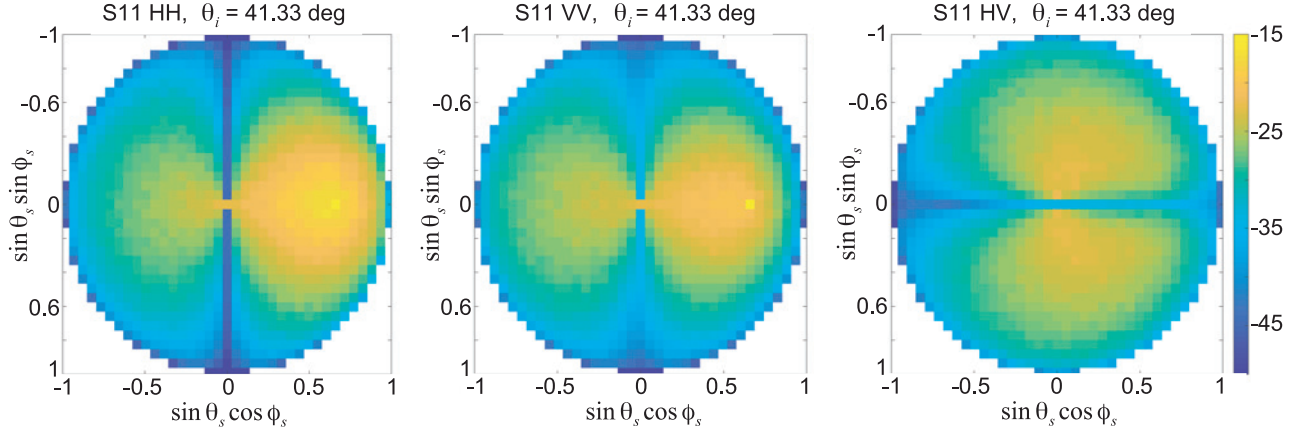


Figure 1. Bistatic scattering pattern example: RMS height = $0.07 \cdot \lambda_0$, lossless media above and below the surface with $\epsilon_r^{(0)} = 1$ and $\epsilon_r^{(1)} = 3$.

$$S_h^{11}(\theta_s, \phi_s; \theta_i, \phi_i) = \sum_{n=1}^N \sqrt{\left(S_{hh}^{11,(n)}(\theta_s, \phi_s; \theta_i, \phi_i)\right)^2 + \left(S_{vh}^{11,(n)}(\theta_s, \phi_s; \theta_i, \phi_i)\right)^2} \quad (3)$$

$$S_v^{11}(\theta_s, \phi_s; \theta_i, \phi_i) = \sum_{n=1}^N \sqrt{\left(S_{hv}^{11,(n)}(\theta_s, \phi_s; \theta_i, \phi_i)\right)^2 + \left(S_{vv}^{11,(n)}(\theta_s, \phi_s; \theta_i, \phi_i)\right)^2} \quad (4)$$

$$S_h^{11}(\theta_s = \theta_i, \phi_s = \phi_i + \pi) = \frac{1}{4} \left(S_h^{11}(\theta_s = \theta_i + \delta\theta_s, \phi_s = \phi_i + \pi) + S_h^{11}(\theta_s = \theta_i - \delta\theta_s, \phi_s = \phi_i + \pi) \right. \\ \left. + S_h^{11}(\theta_s = \theta_i, \phi_s = \phi_i + \pi + \delta\phi_s) + S_h^{11}(\theta_s = \theta_i, \phi_s = \phi_i + \pi - \delta\phi_s) \right) \quad (5)$$

$$S_v^{11}(\theta_s = \theta_i, \phi_s = \phi_i + \pi) = \frac{1}{4} \left(S_v^{11}(\theta_s = \theta_i + \delta\theta_s, \phi_s = \phi_i + \pi) + S_v^{11}(\theta_s = \theta_i - \delta\theta_s, \phi_s = \phi_i + \pi) \right. \\ \left. + S_v^{11}(\theta_s = \theta_i, \phi_s = \phi_i + \pi + \delta\phi_s) + S_v^{11}(\theta_s = \theta_i, \phi_s = \phi_i + \pi - \delta\phi_s) \right) \quad (6)$$

The first step to parametrize the datacube is to parametrize the bistatic scattering patterns shown in Figure 1. Observing the patterns, there are two ‘irregular’ features making pattern parametrization difficult: 1) bipolar-like patterns due to projecting the scattered energy to polarized components, resulting in dips along the axis where the scattering polarization is perpendicular to the incident polarization; and 2) the specular components in the co-polarization scattering patterns, which are prominent and outlier-like for surfaces with small to medium roughness. To facilitate modeling, we first combine the H - and V -polarized scattering patterns from the Monte Carlo simulations and average them over all realizations, using Eq. (3) and Eq. (4), where N is the number of realizations. The polarization-combined patterns can be viewed as the energy patterns scattered from the rough surface in responding to the H -polarized or the V -polarized incidence. With the model we developed in this work, we can reconstruct the polarization-combined patterns for the given surface roughness and dielectric properties. The polarized patterns are computed by splitting the energy of the polarization-combined patterns based on the projection of the outgoing and incoming polarizations. This is an approximation that is discussed further in Section 3.

Next, we treat the specular scattering coefficients as outliers by removing them from the polarization-combined patterns and replacing them with the average of the scattering coefficients of the adjacent directions, using Eq. (5) and Eq. (6). Since the specular scattering coefficients have been calculated accurately by the SEBCM, we retain them in a look-up table [22], which takes very small storage space compared to the datacube. They can be inserted back to the reconstructed bistatic patterns through interpolation.

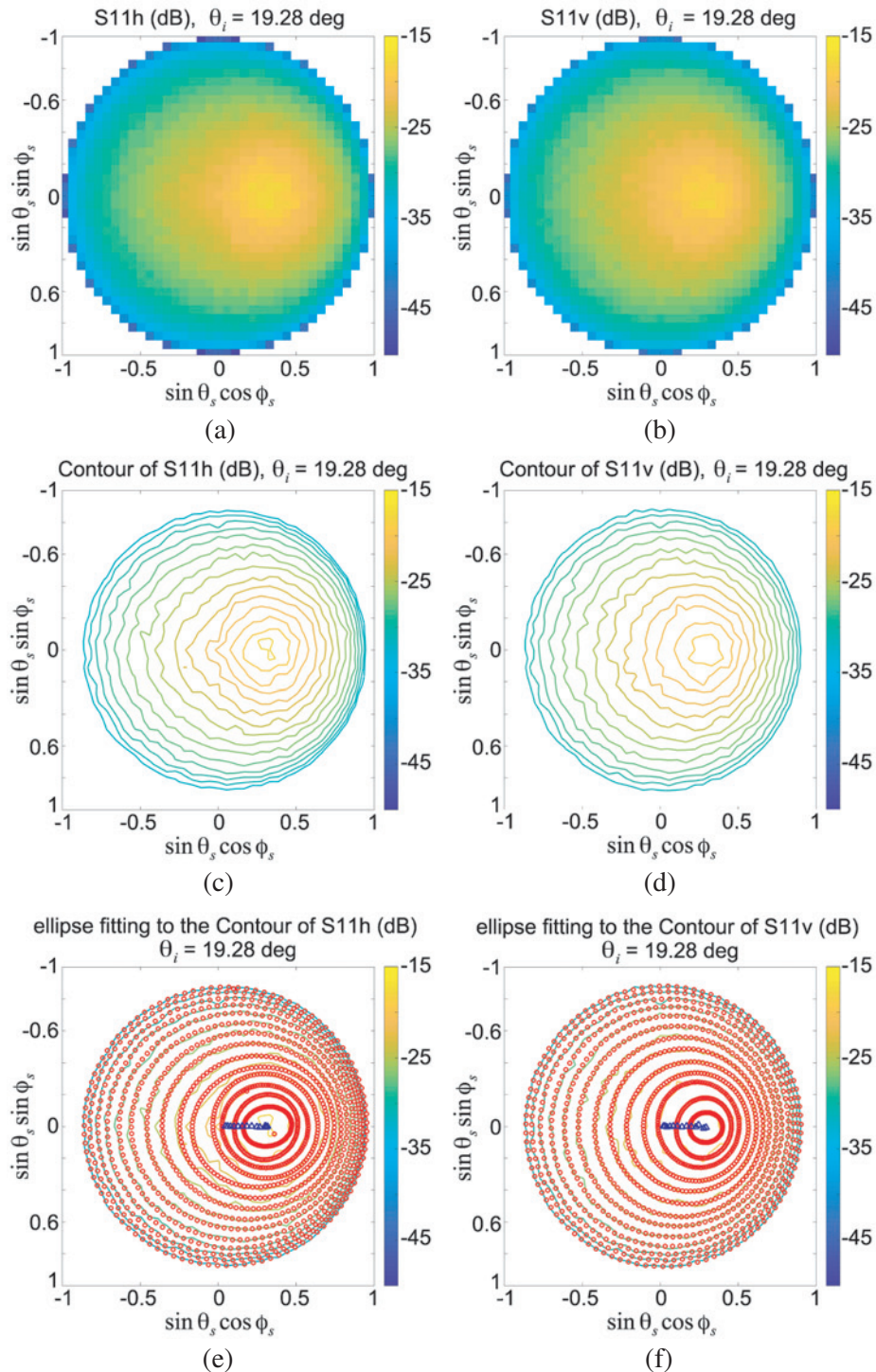


Figure 2. Scattering distribution example at one scattering direction. Left: scattering coefficient magnitudes follow a Rayleigh distribution; Right: scattering coefficient phases follow uniform distribution.

2.2. Pattern Fitting

It is observed that, in Figures 3(a) and (b) for the H -pol and the V -pol incidences respectively, the polarization-combined bistatic patterns can be approximated by a group of nested contours at the

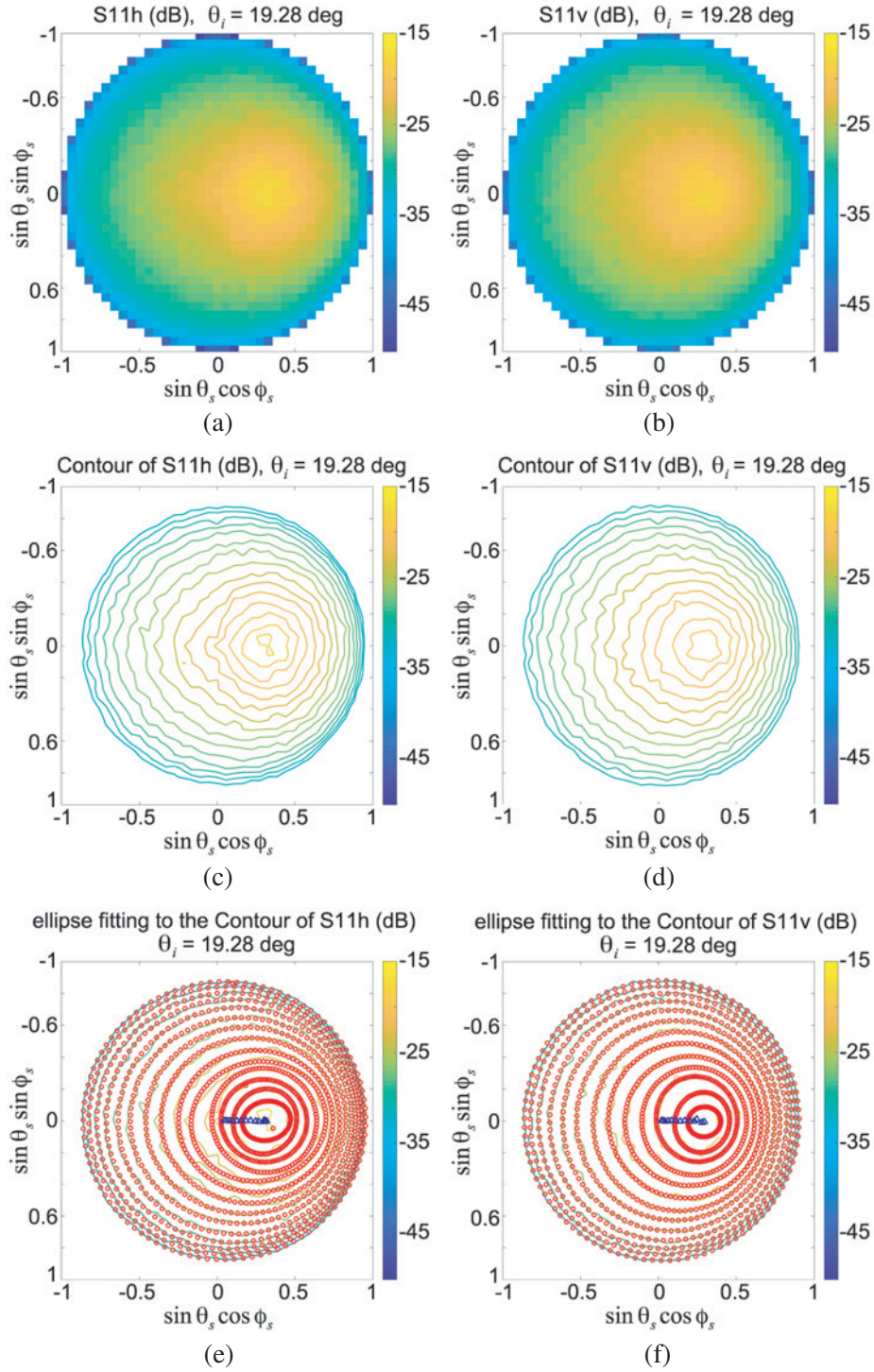


Figure 3. Bistatic scattering pattern analysis example for a case with rms height of $0.07\lambda_0$, $\epsilon_r^{(0)} = 1$, $\epsilon_r^{(1)} = 3$, and incident angle of 19.28° : (a) and (b) are polarization-combined patterns after specular coherence removal for H and V incidence, respectively; (c) and (d) are contour approximation of the patterns in (a) and (b); (e) and (f) are ellipse fitting of the contours in (c) and (d), with red circles marking the ellipses and blue triangles marking the center of the ellipses.

discrete magnitude levels as shown in Figures 3(c) and (d). These contours are well-approximated by ellipses as shown in Figures 3(e) and (f). Each elliptical contour can be described by five parameters, which are its magnitude level, center in the k_x - and the k_y -direction relative to the origin of the normalized k -space, and its elliptical major and minor axis lengths in the normalized k -space. These parameters vary as a function of the surface roughness, surface dielectric contrast, and incident angle. By further fitting the dependence of these parameters across the surface properties and incident angle, we can build a model consisting of a set of analytical and look-up functions. The model can then be quickly run in reverse, so that, given the rough surface properties, medium dielectric, and the incident angle, we are able to reconstruct the ellipses and form the pattern contours, thereby reconstructing the pattern and compute the average bistatic scattering coefficient in the scattering direction of interest quickly.

We also reduce the number of elliptical parameters from five to three based on two observations. First, as seen in Figures 3(e) and (f), the center shift (marked by blue triangles) happens generally along the incident direction, i.e., within the incidence plane, which is physically intuitive. Therefore, we assume that the center shift is always zero in the k_y -direction. Second, by examining the axes of ellipses resulting from an initial fitting of the S_{11} polarization-combined patterns, we find that their major and minor axes are nearly equal at all incident angles for V -pol incidence and at lower incident angles for H -pol incidence, as shown in Figure 4. Therefore, we assume from the start that the major

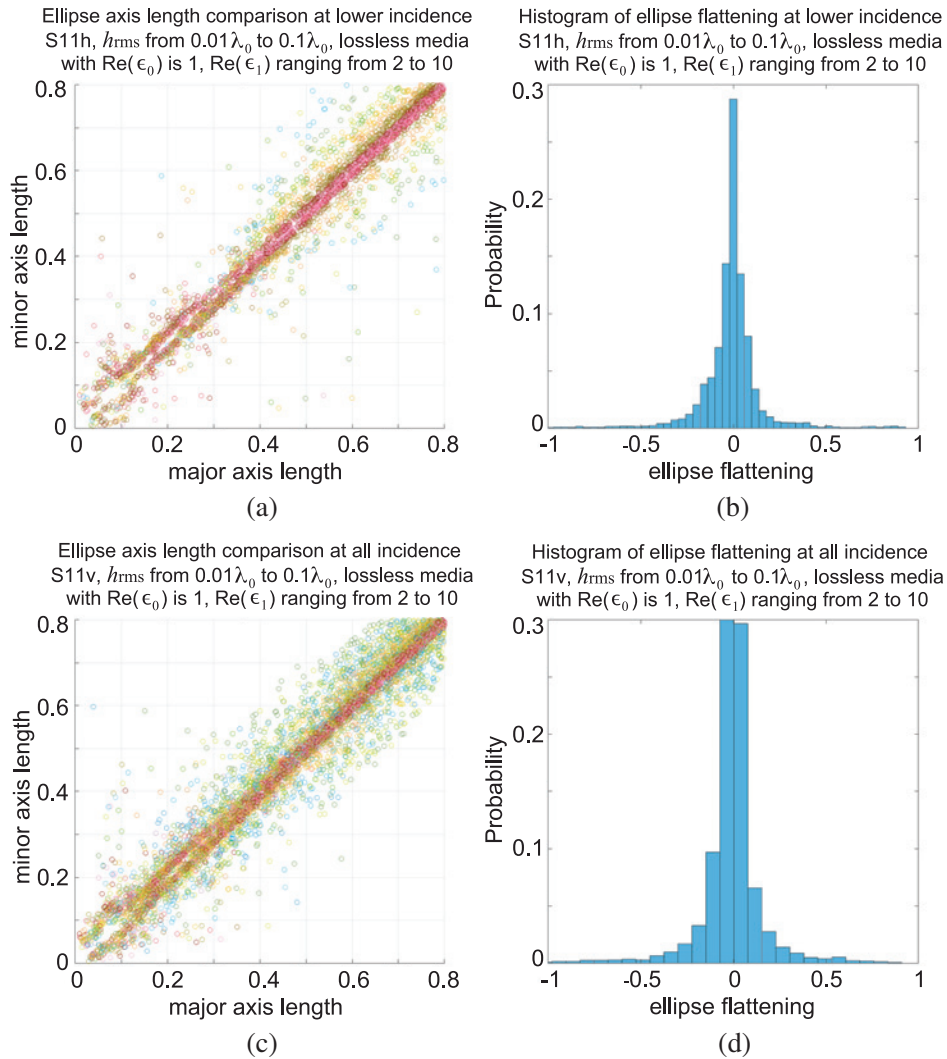


Figure 4. Ellipse axis length comparison for S_h^{11} ((a) and (b)) and S_v^{11} ((c) and (d)): (a) and (c) are scatter plots of major axis length vs. minor axis length; (b) and (d) are ellipse flattening histograms.

and minor axes of the ellipses are equal in length, and so the contours are simply approximated as circles. Figures 4(b) and (d) show the histograms of ellipse flattening, which is defined as the length difference between the major and minor axes over the major axis length. Additionally, at near grazing incident angles, the polarization-combined pattern of H -pol incidence becomes bipolar and cannot be approximated by nested ellipses any more. Addressing the bipolar pattern is not in the scope of this work.

With those two assumptions, the three parameters describing each elliptical (or circular) contour are its contour magnitude level L , in-plane center shift Δ , and its major axis length (or radius) A . These three parameters do not vary independently from one another, therefore we require one of the three parameters to serve as a reference for the other two parameters, so that the three parameters can be linked to describe a group of contours that form a pattern. We chose the contour magnitude level in dB as the reference. As observed in the scattering pattern, the range of the contour levels, which is confined by upper and lower bounds, depends on both the surface properties and the incident angle. Therefore, we first model the bounds of the level range as a function of the incident angle; then next model the coefficients of the function with respect to the surface properties. The contour radii and their center shifts are then modeled with respect to the normalized contour level as well as the incident angles as analytical functions, the coefficients of which are fitted as functions of the surface properties. In summary, the fitting procedure uses a nested parametrization that begins with the normalized contour levels described next.

2.2.1. Modeling the Contour Level Bound

The upper and lower level bounds (in dB) of the H -pol and V -pol incidences have generally an exponential dependence on the sine of the incident angle (i.e., $\sin \theta_i$), as shown in Figure 5 for example. This exponential dependence can be expressed in the form of Eq. (7). In the cases of the upper level bound of the V -pol incidence (Figure 5(b)) and the lower level bound of the H -pol incidence (Figure 5(c)), the level increases as the incident angle decreases and approaches zero, which can be expressed by an exponential function as well. Hence, for the lower level bound of the H -pol incidence and the upper level bound of the V -pol incidence, a pair of exponential functions are used in two sections to capture the level dependence on incident angle. We use θ_{break} to note the break point between the two sections.

$$L^{(dB)} = a_L \cdot \exp(b_L \cdot \sin \theta_i) + c_L \quad (7)$$

To facilitate the expression of the dependence of the coefficients a_L , b_L , and c_L in Eq. (7) on the surface properties, we introduced here the effective surface roughness h_{eff} and the dielectric contrast s . The effective surface roughness h_{eff} is defined as the roughness per wavelength in the medium as $h_{\text{eff}} = h_0 \cdot \sqrt{\epsilon_r^{(0)}}$, where h_0 is the free space rms height per free space wavelength. The dielectric contrast s is defined as $s = (\epsilon_r^{(1)} - \epsilon_r^{(0)}) / (\epsilon_r^{(1)} + \epsilon_r^{(0)})$. Because we only model media with $\epsilon_r^{(0)} < \epsilon_r^{(1)}$, the dielectric contrast is here always positive, $s > 0$.

Fitting the coefficients a_L , b_L , and c_L of the exponential functions (in the form of Eq. (7)) with respect to the surface roughness and dielectric properties is performed for the four bounds individually as presented below. Overall, the coefficient a_L for all level bounds, except the section where $\theta_{inc} < \theta_{break}$ for the lower level bound of the H -pol incidence and the upper level bound of the V -pol incidence, shows dependence on both the surface roughness and dielectric contrast, and the dependence can be approximately separated. Dependence of a_L on roughness can be expressed by an analytical form in Eq. (8).

$$a_L = q \cdot \exp\left(a_L^{(1)} \cdot h_{\text{eff}}\right) + a_L^{(2)} \quad (8)$$

where coefficients $a_L^{(1)}$ and $a_L^{(2)}$ are functions of the dielectric contrast. They can be approximated by either an exponential function in Eq. (9) or a linear function in Eq. (10).

$$\xi = \xi_1 \cdot \exp(\xi_2 \cdot s) + \xi_3 \quad (9)$$

$$\xi = \xi_1 \cdot s + \xi_2 \quad (10)$$

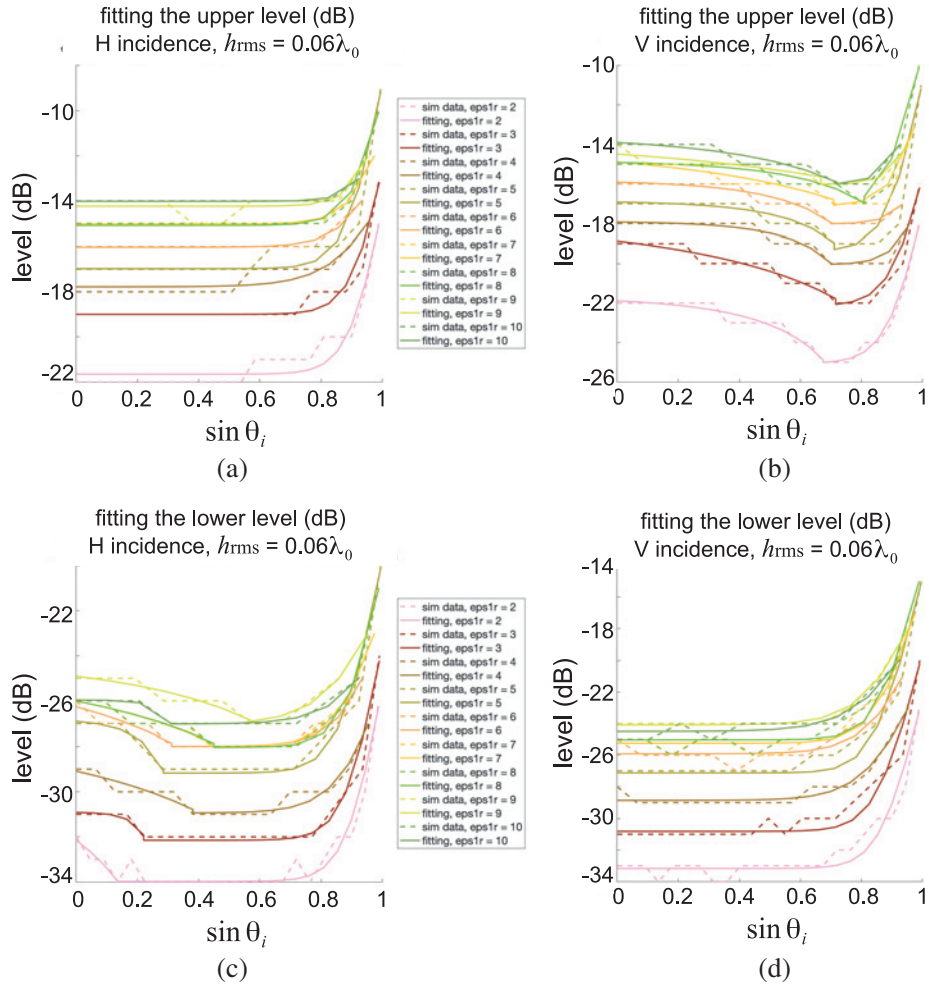


Figure 5. Fitting the upper bound ((a) and (c)) and the lower bound ((b) and (d)) of the circular contour levels as a function of incident angle (example of rms height of $0.06\lambda_0$). In the case of the lower bound fitting for H -pol incidence and the upper bound fitting for V -pol incidence, two-section fitting is used.

Table 2 lists the values and formulas used for computing the above coefficients. In the case of two-section functions for the lower level bound of the H -pol incidence and the upper level bound of the V -pol incidence, coefficient a for the section where $\theta_{inc} < \theta_{break}$ can be approximated as a constant, values of which are reported in Table 2 as well.

The coefficient b_L in Eq. (7) mainly depends on the dielectric contrast and has little dependence on the surface roughness. Its dependence on the dielectric contrast can be expressed analytically as Eq. (11) and does not vary significantly between the four bounds.

$$b_L = 9 \cdot s + 12.5 \quad (11)$$

The coefficient c_L depends on both the surface roughness and the dielectric contrast. Its dependence in some cases, e.g., for the upper bound of the H -pol incidence (Figure 5(a)) and the lower bound of the V -pol incidence (Figure 5(f)), can potentially be approximated by analytical functions. However, for lower bound of H -pol and upper bound of V -pol, which need two-section expressions, analytical approximation has large residual error, especially for the smaller incidence angles. Hence, for better accuracy, instead of using analytical functions, we use look-up tables [22], which are directly formed through interpolation of the datacube. Figures 6(a) and (f) show the dependence of the coefficient c_L in Eq. (7) on the roughness and the dielectric contrast for the upper bound of H -pol incidence and

Table 2. Formula and coefficients for computing coefficient a in Eq. (7).

	upper bound H -pol inc	lower bound H -pol inc	upper bound V -pol inc	lower bound V -pol inc
two-section formula of Eq. (7)	no	yes	yes	no
	all θ_{inc}	$\theta_{\text{inc}} \geq \theta_{\text{break}}$	$\theta_{\text{inc}} \geq \theta_{\text{break}}$	all θ_{inc}
	Eq. (8)	Eq. (8)	Eq. (8)	Eq. (8)
coefficient a_L for └ formula of a_L	-18.4472	-8.3745	-18.9565	-7.6905
└ coefficient q				
└ cocoefficient $a_L^{(1)}$ └ formula of $a_L^{(1)}$	Eq. (9)	Eq. (10)	Eq. (9)	Eq. (9)
└ coefficient ξ_1	-0.5278	-19.7253	-95.1705	-7.1549
└ coefficient ξ_2	4.9727	-9.0144	0.1577	2.2346
└ coefficient ξ_3				
└ coefficient $a_L^{(2)}$ └ formula of $a_L^{(2)}$	-7.9231	(NA)	92.0372	-1.5924
└ coefficient ξ_1				
└ coefficient ξ_2	Eq. (10)	Eq. (10)	Eq. (10)	Eq. (10)
	-38.9105	-23.2616	-48.4865	-20.1584
	-61.8084	-83.5696	-57.2051	-82.8580
coefficient a_L for └ coefficient a_L	(NA)	$\theta_{\text{inc}} < \theta_{\text{break}}$	$\theta_{\text{inc}} < \theta_{\text{break}}$	(NA)
	(NA)	-2.7541×10^{-6}	-2.3044×10^{-6}	(NA)

the lower bound of V -pol incidence, respectively. For the lower bound of H -pol incidence, Figure 6(b) shows the coefficient c_L of its exponential function section where $\theta_{\text{inc}} > \theta_{\text{break}}$, and Figure 6(c) shows the coefficient c_L for the section where $\theta_{\text{inc}} < \theta_{\text{break}}$. Similarly, Figures 6(d) and (e) show the coefficient c_L of the two-section function of the upper bound of V -pol incidence.

2.2.2. Modeling the Contour In-Plane Center Shift

The center shifts within the incidence plane of the elliptical (or circular) contours are mainly driven by the incident angle. Figure 7 shows an example of the in-plane center shifts with respect to the normalized contour level L_N , which is the contour level normalized by the lower bound for individual incident angles at the given surface properties. For each incident angle, the curves in Figure 7 shows the contour center moving from roughly zero to the point of projecting the normalized specular k -vector to the normalized (k_x, k_y) plane. At small roughnesses, the centers of the contours remain around zero in the normalized (k_x, k_y) plane; as the surface roughness increases, the range of the contour level increases and the center of the high level contour gets closer to the specular direction. Hence, as the surface roughness increases, the curves extend to higher contour level regime with little change in their shape. The impact of the dielectric contrast on the in-plane center shift was found to be negligible.

To model these curves, we again fit them with the exponential function of the form in Eq. (12) for each incident angle. At large roughnesses, it is observed that the center shift increases slowly when the

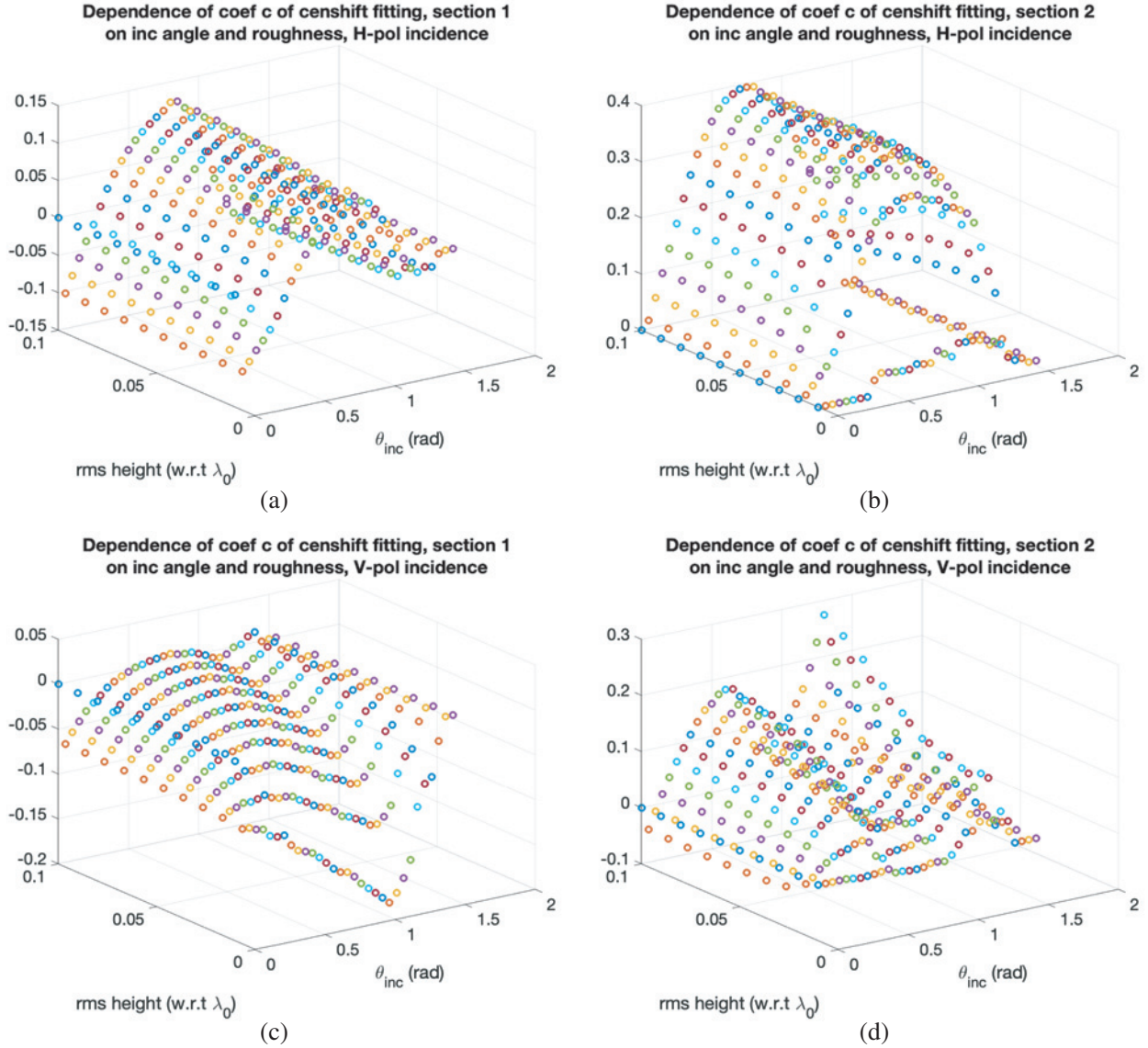


Figure 6. Dependence of the coefficient c on the effective roughness and the dielectric contrast, from fitting the bounds of the circular contour levels as a function of incident angles [22]: (a) coefficient c from fitting the upper level bound of H -pol incidence; (b) and (c) coefficient c from fitting the lower level bound of H -pol incidence; (d) and (e) coefficient c from fitting the upper level bound of V -pol incidence; (f) coefficient c from fitting the lower level bound of V -pol incidence.

normalized contour level is larger than a threshold level $L_T = 7$ dB. Hence, we combine two sections of exponential functions to fit the curve more accurately.

$$\Delta = a_{\Delta} \cdot \exp(b_{\Delta} \cdot L_N) + c_{\Delta} \tag{12}$$

The coefficient a_{Δ} and b_{Δ} depend only on the incident angle, and have little dependence on surface roughness. The coefficient a_{Δ} for the H -pol incidence as found to be,

$$\begin{cases} a_{\Delta,h} = -0.0393 \cdot \theta_{inc} + 0.1026, & \text{for } L_N < L_T \\ a_{\Delta,h} = -0.0064 \cdot \theta_{inc} + 0.0151, & \text{otherwise} \end{cases} \tag{13}$$

and for the V -pol incidence,

$$\begin{cases} a_{\Delta,v} = -0.0242 \cdot \theta_{inc} + 0.0651, & \text{for } L_N < L_T \\ a_{\Delta,v} = -0.0380 \cdot \theta_{inc} + 0.0449, & \text{otherwise} \end{cases} \tag{14}$$

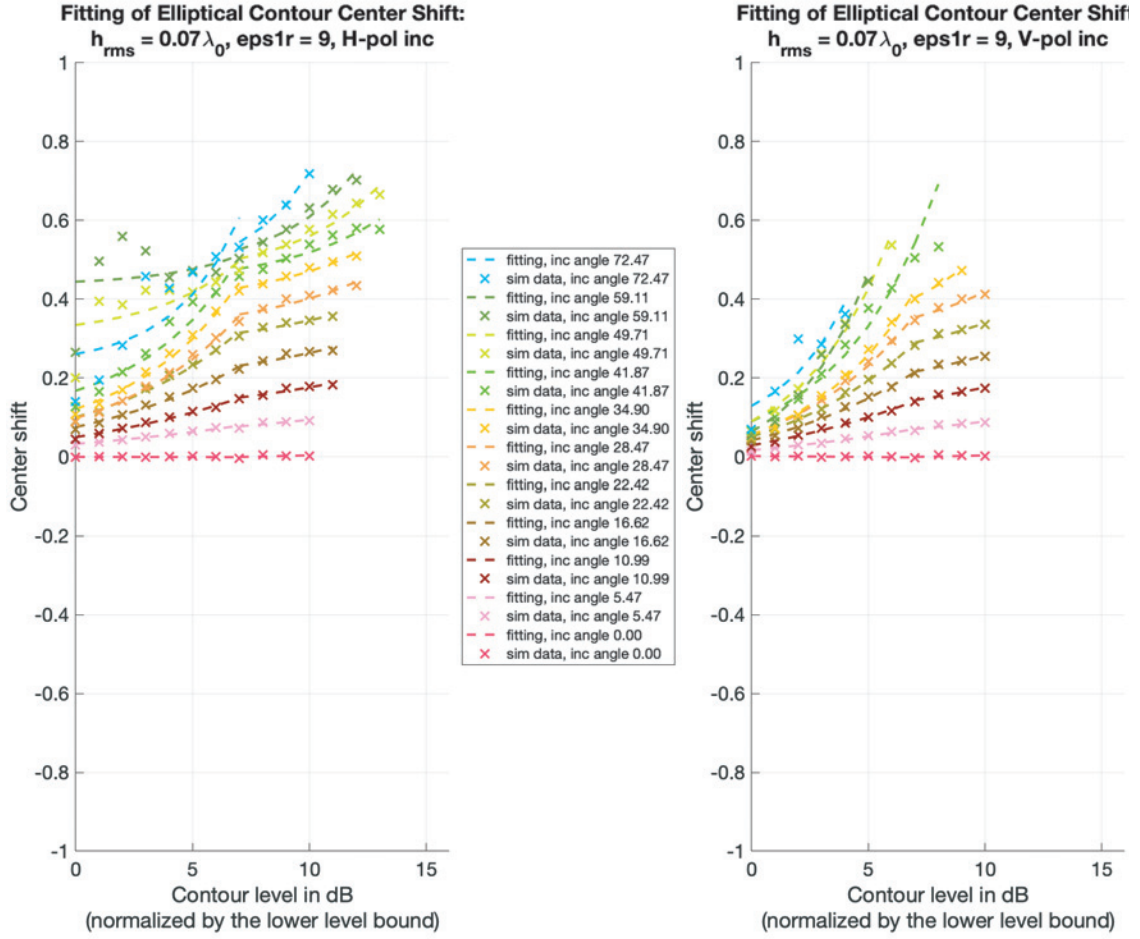


Figure 7. Fitting the elliptical contour center shift as a function of normalized contour level: example shown for rms height of $0.07\lambda_0$ and $\epsilon^{(1)} = 9$. Two-section fitting is needed with break point at $L_T = 7$ dB.

The coefficient b_{Δ} can be expressed by Eq. (15) for both the H -pol and V -pol incidences.

$$b_{\Delta,h} = b_{\Delta,v} = 0.2406 \cdot \theta_{\text{inc}} + 0.0612 \quad (15)$$

The coefficient c_{Δ} in Eq. (12) are kept as look-up functions with respect to incident angle and surface roughness, and are plotted in Figure 8. Models of all coefficients depend on the angle of incidence; only the coefficient c_{Δ} reflects the slight dependence on the surface roughness.

2.2.3. Modeling the Elliptical Contour Major Axis Length (or the Circular Contour Radius)

The major axis lengths of the elliptical contours, or the radii of the simplified circular contours, are mainly driven by the surface roughness, and their dependence on the normalized contour level L_N also depends on the angle of incidence. The effect of surface dielectric contrast has mostly been captured by the contour level models. Shown in Figure 9 for example, the major axis length is plotted with respect to the normalized contour level for each available incident angle, to which we fit an exponential function in the form of Eq. (16).

$$A = a_A \cdot \exp(b_A \cdot L_N) + c_A \quad (16)$$

Both the coefficients a_A and c_A vary largely as surface roughness or incident angle changes, while the coefficient b_A has little variation as a function of surface roughness, and can be expressed by a linear function of incident angle as

$$b_A = 0.0902 \cdot \theta_{\text{inc}} + 0.1246 \quad (17)$$

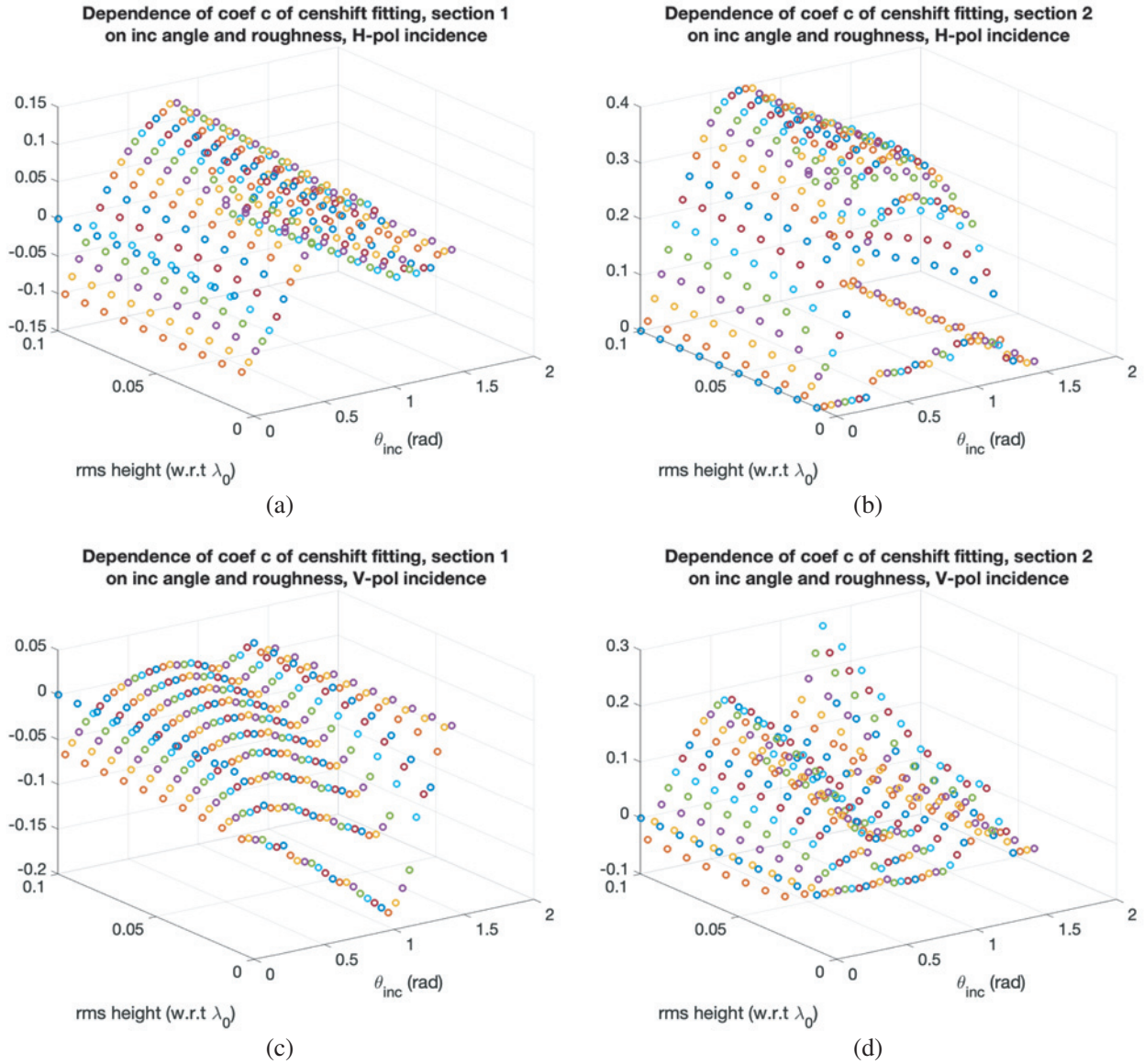


Figure 8. Dependence of the coefficient c on the roughness and the incident angle, from fitting the center shifts of the circular contours as a function of normalized contour level [22]: (a) and (b) for H -pol incidence; (c) and (d) are for V -pol incidence.

For coefficients a_A and c_A , their dependence on the surface roughness and the angle of incidence can be approximately separated. We first fit their dependence on the incident angle using the 2nd order polynomial function as shown in Eq. (18), where ξ_A represents a_A or c_A .

$$\xi_A = \xi_A^{(2)} \cdot \theta_{inc}^2 + \xi_A^{(1)} \cdot \theta_{inc} + \xi_A^{(0)} \tag{18}$$

The polynomial coefficients are further fitted with higher order polynomial function of the surface roughness h_{eff} as

$$\xi_A^{(n)} = p_4 \cdot h_{eff}^4 + p_3 \cdot h_{eff}^3 + p_2 \cdot h_{eff}^2 + p_1 \cdot h_{eff} + p_0 \tag{19}$$

where $n = 0, 1, 2$. The quartic function coefficients for $a_A^{(n)}$ and $c_A^{(n)}$ are listed in Table 3 and Table 4, respectively.

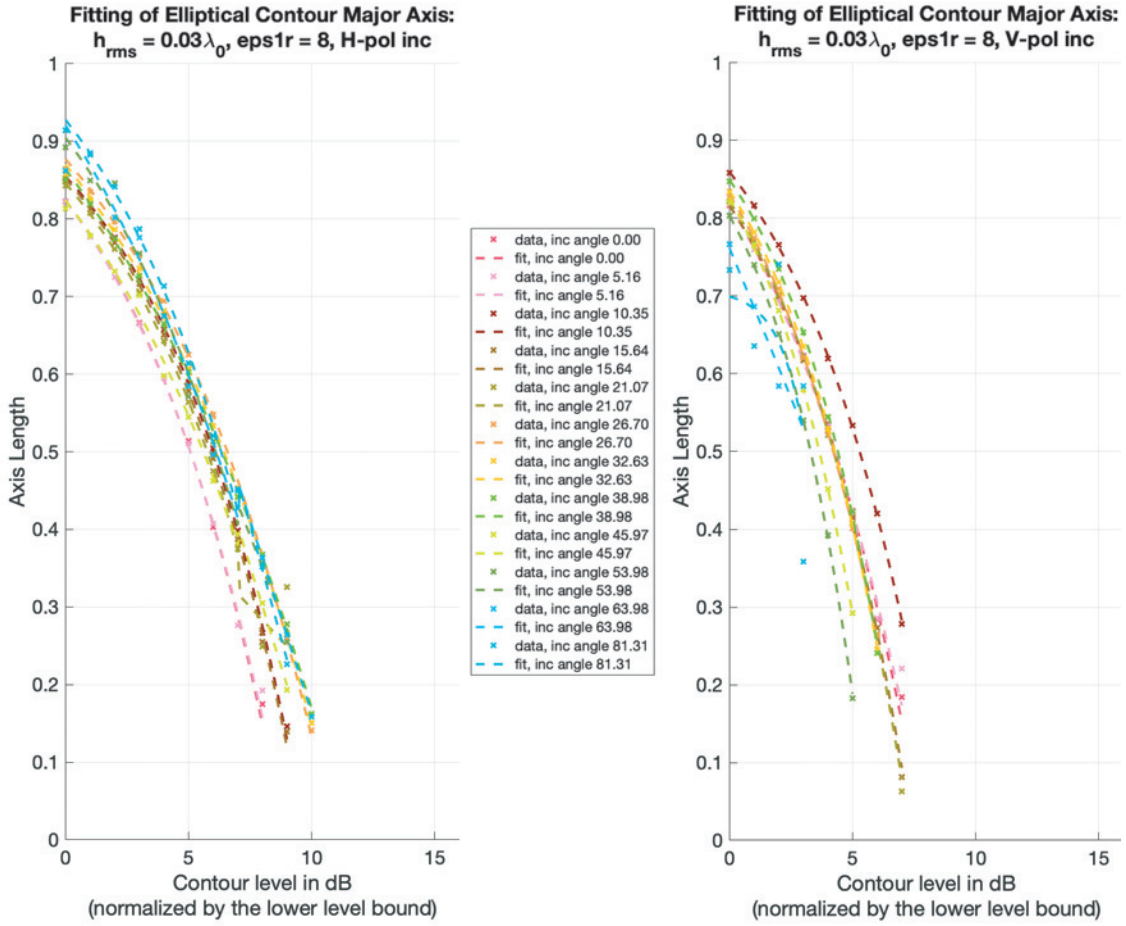


Figure 9. Fitting the major axes of the elliptical contours as a function of normalized contour level.

Table 3. Coefficient values of quartic functions for $a_A^{(2)}$, $a_A^{(1)}$, and $a_A^{(0)}$ for H -pol and V -pol incidence.

Coefficient	p_4	p_3	p_2	p_1	p_0
$a_{A,h}^{(2)}$	36.5520	-15.2655	-8.6889	1.5809	-0.2739
$a_{A,v}^{(2)}$	269.4968	-195.5572	40.3816	-2.6855	-0.0780
$a_{A,h}^{(1)}$	208.2550	-188.3767	-78.9353	-9.9852	0.8031
$a_{A,v}^{(1)}$	-116.3462	27.7872	22.4430	-5.1314	0.4474
$a_{A,h}^{(0)}$	-534.5934	415.0397	-124.7737	14.3350	-0.7864
$a_{A,v}^{(0)}$	-618.1680	486.9267	-138.1610	15.4456	-0.7741

3. BISTATIC SCATTERING PATTERN RECONSTRUCTION AND RESULTS

Reconstruction of the bistatic scattering patterns can be done through the process diagrammed in Figure 10. The three green boxes mark reconstruction of the contour level range, the contour center location shifts, and the contour radii through the core models described in Section 2.2.1, 2.2.2, and 2.2.3. In the reconstruction process, the contour level bounds are first computed from the input parameters, which are again the polarization of the incidence field (H -pol or V -pol), incident angle θ_{inc} , surface rms

Table 4. Coefficient values of quartic functions for $c_A^{(2)}$, $c_A^{(1)}$, and $c_A^{(0)}$ for H -pol and V -pol incidence.

Coefficient	p_4	p_3	p_2	p_1	p_0
$c_{A,h}^{(2)}$	-35.8565	34.3756	-5.3137	2.0069	0.3279
$c_{A,v}^{(2)}$	577.3304	-223.5262	15.7901	1.4796	0.0071
$c_{A,h}^{(1)}$	87.8210	14.4259	-37.2507	4.0670	-0.8097
$c_{A,v}^{(1)}$	-513.6674	312.9912	-83.5511	9.5642	-0.3889
$c_{A,h}^{(0)}$	398.3191	-373.1519	130.9803	-16.3038	1.7070
$c_{A,v}^{(0)}$	754.0062	-602.3096	174.4451	-19.7744	1.6968

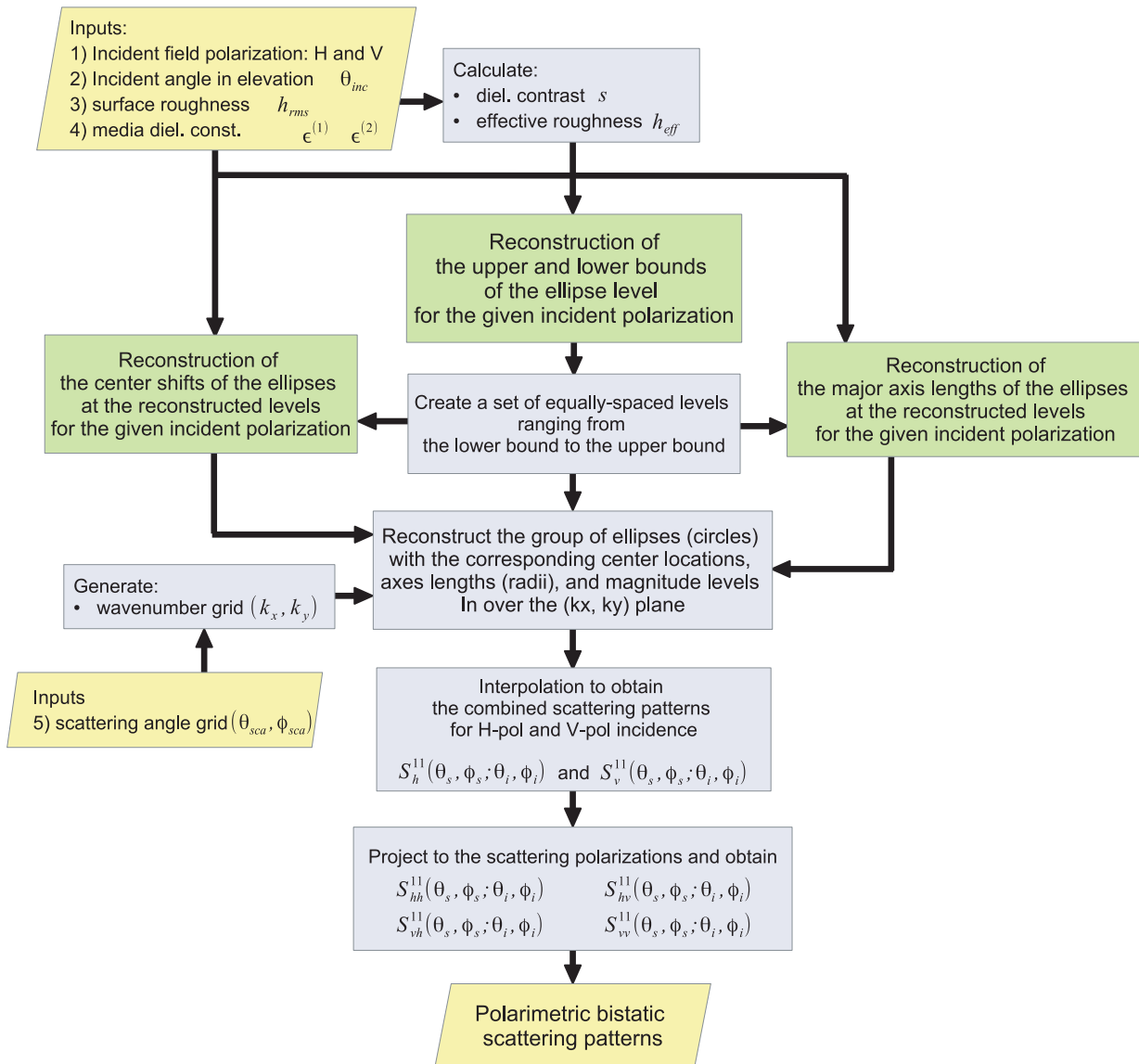


Figure 10. Flow chart of bistatic scattering pattern reconstruction.

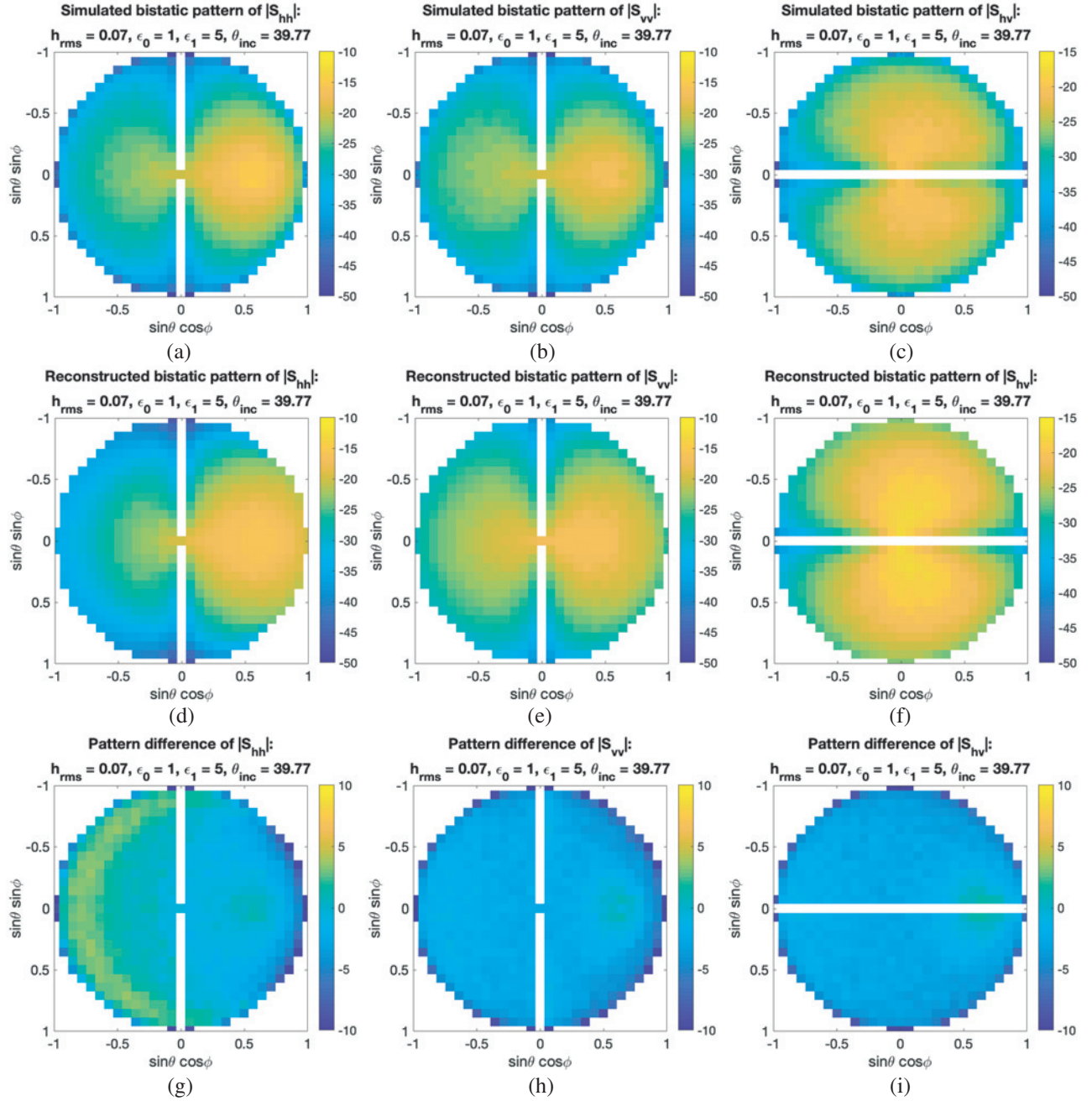


Figure 11. One example of comparison of the reconstructed and the simulated polarimetric bistatic scattering patterns of the HH , VV , and HV components (surface rms height $h_{\text{rms}} = 0.07 \cdot \lambda_0$, dielectric constants are $\epsilon^{(0)} = 1$ and $\epsilon^{(1)} = 5$ for above and below the surface, respectively. The incident angle is about 40°): (a)–(c) are the original scattering patterns simulated using SEBCM; (d)–(f) are reconstructed scattering patterns; (g)–(i) are the differences by subtracting the reconstructed patterns from the original patterns. The averaged differences are 1.94 dB in HH , 2.66 dB in HV , and 3.04 dB in VV .

height h_{rms} , and dielectric constants above ($\epsilon^{(1)}$) and below ($\epsilon^{(2)}$) the rough surface. An equally-spaced level set (in dB) is then created ranging from the contour level lower bound to the upper bound, which is then one of the inputs to the reconstructions of the contour center location shifts and the contour radii. Together with the above mentioned input parameters, the contour center shifts and radii are computed

relative to the $(\tilde{k}_x, \tilde{k}_y)$ plane in the normalized k -space, i.e., $\tilde{k}_x = \sin \theta_s \cos \phi_s$ and $\tilde{k}_y = \sin \theta_s \sin \phi_s$.

Given the scattering directions of interest in terms of (θ_s, ϕ_s) , we can construct the $(\tilde{k}_x, \tilde{k}_y)$ grid in the normalized k -space and recreate the circular contours knowing their levels, center locations, and radii. Interpolation is then applied to further smooth the pattern. Splitting the combined scattering pattern to the H -pol and the V -pol components cannot be rigorously calculated by the current model, which requires additional information on energy ratio between polarizations to be parametrized. Instead, the current model simply projects the outgoing scattering polarization vectors to the incident polarization vector to further decompose the scattering coefficients to the H -pol and the V -pol components. Thereby, the polarimetric bistatic scattering patterns $S_{hh}^{11}(\theta_s, \phi_s; \theta_i, \phi_i)$ and $S_{vh}^{11}(\theta_s, \phi_s; \theta_i, \phi_i)$ are reconstructed for the H -pol incidence, and $S_{vv}^{11}(\theta_s, \phi_s; \theta_i, \phi_i)$ and $S_{hv}^{11}(\theta_s, \phi_s; \theta_i, \phi_i)$ for the V -pol incidence. The scattering coefficients at the specular directions are then replaced by the values from interpolation of the specular coefficient look-up table [22]. For evaluating the pattern

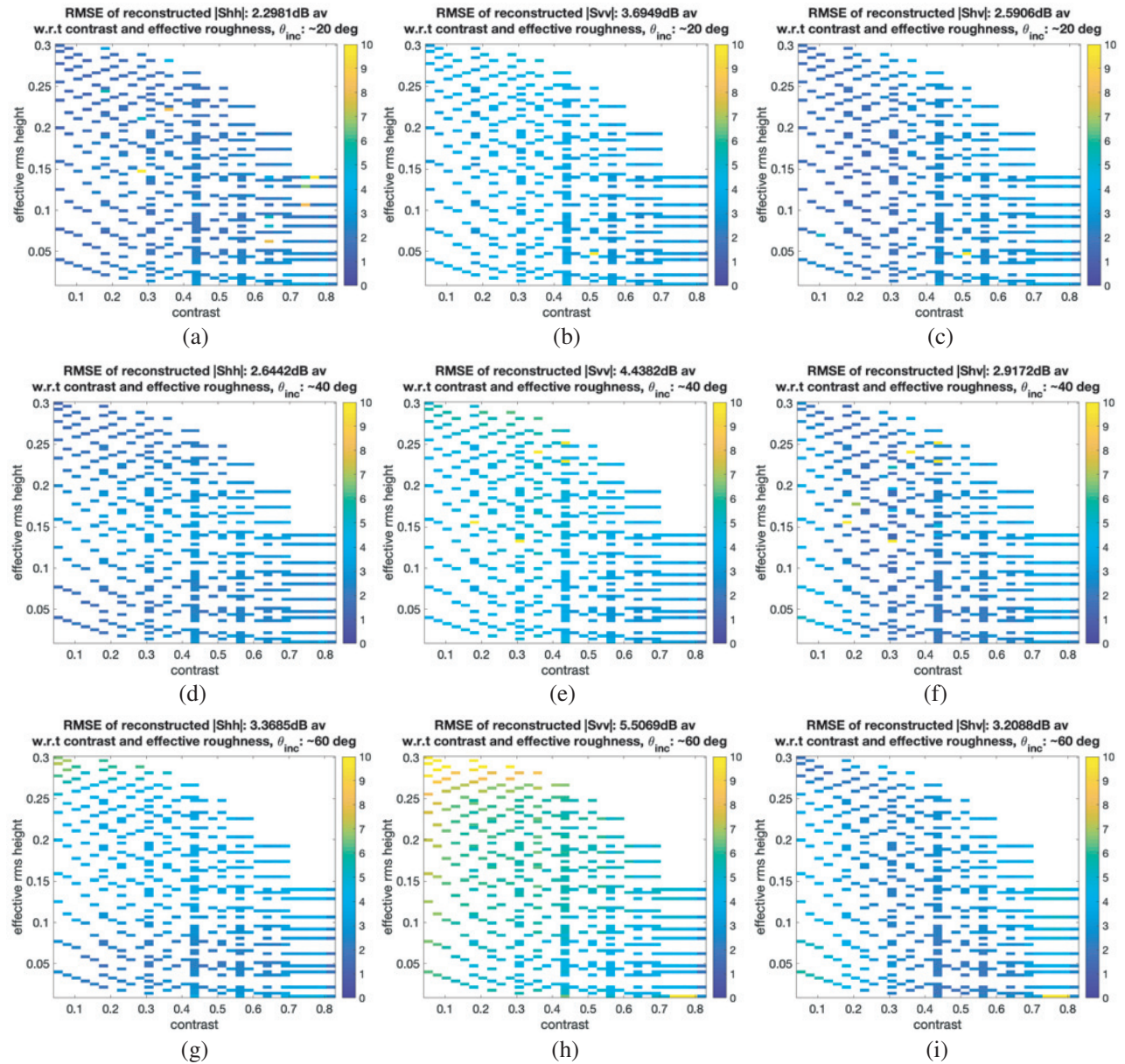


Figure 12. RMSE between the original and the reconstructed bistatic patterns as a function of the contrast and the effective rms height: 1) (a) to (c) are at small incident angle near 20°; 2) (d) to (f) are at middle incident angle near 40°; 3) (g) to (i) are at large incident angle near 60°.

reconstruction performance using the parametrization-based model, below we compare only the patterns before restoring the specular scattering coefficients.

Figure 11 shows an example of the reconstructed patterns compared to the original patterns simulated using SEBCM. The reconstructed bistatic scattering coefficients are in good agreement to the original ones; their differences are shown in Figures 11(g) to (i), which are computed by subtracting the reconstructed patterns from the original patterns. It can be seen from the example that the reconstructed patterns tend to underestimate the scattering around the specular direction and overestimate the scattering at the larger incident angles in elevation, except in the backscatter half of the HH pattern. By averaging over all scattering directions, the differences are 1.94 dB in HH , 2.66 dB in HV , and 3.04 dB in VV .

For all the cases we simulated with $\epsilon^{(0)} < \epsilon^{(1)}$ for the datacube, the RMSEs between the original and the reconstructed bistatic scattering patterns are calculated and displayed in Figure 12 as a function of contrast s and the effective rms height h_{eff} for three incident angles ($\theta_i = 20^\circ$, 40° , and 60°). The averaged RMSEs over contrast and roughness are also shown as a function of incidence angle in Figure 13. Overall, the bistatic scattering patterns are reconstructed with fairly good accuracy. Errors are bigger in the VV patterns compared to those for the HH and the HV patterns. Also, the reconstructed patterns becomes less accurate as the incident angle approaches grazing angles, especially in the cases with larger roughness and lower contrast.

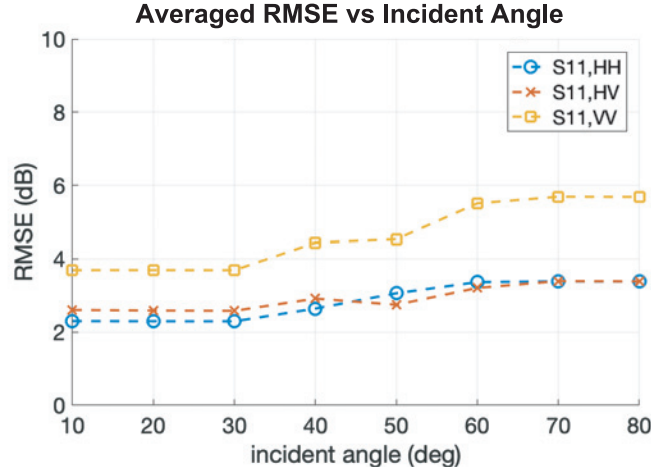


Figure 13. Averaged RMSE over the angle of incidence. This shows that the reconstruction error increases as a the incidence angle approaches grazing.

So far, we have only considered scattering from a lossless subsurface. For the lossy cases, we first compare their bistatic scattering patterns with those of their corresponding lossless cases; both are simulated using the SEBCM3D. Their averaged differences are plotted in Figure 14 as a function of the imaginary part of the lower medium dielectric constant for different roughness and the real part of the lower medium dielectric constant. We expect to see the difference between the lossless and the lossy patterns increases as the loss in the lower medium increases; and this difference is observed to be smaller when the lower medium dielectric constant has a larger real part. Overall, within the amount of medium loss considered in this work, the difference between the lossless and the lossy patterns turns out to be smaller than the pattern reconstruction error. Hence, we use the same model for pattern reconstruction for the lossy cases. If in future parametrization-based models, the reconstruction accuracy was improved, then investigating the lossy cases can be revisited. In addition, though expected to be small, the effect of the upper medium loss is not evaluated in this work, as we are mainly concerned with bistatic patterns in which the top surface is beneath air or free space.

Compared to simulation of the bistatic scattering patterns using SEBCM3D, which takes about 1.8 CPU hours on average for computing one surface realization in the Monte Carlo process, the parametrization-based model can reconstruct the patterns within a fraction of a second. Though, in many cases, the reconstructed patterns might be less accurate than patterns computed by models

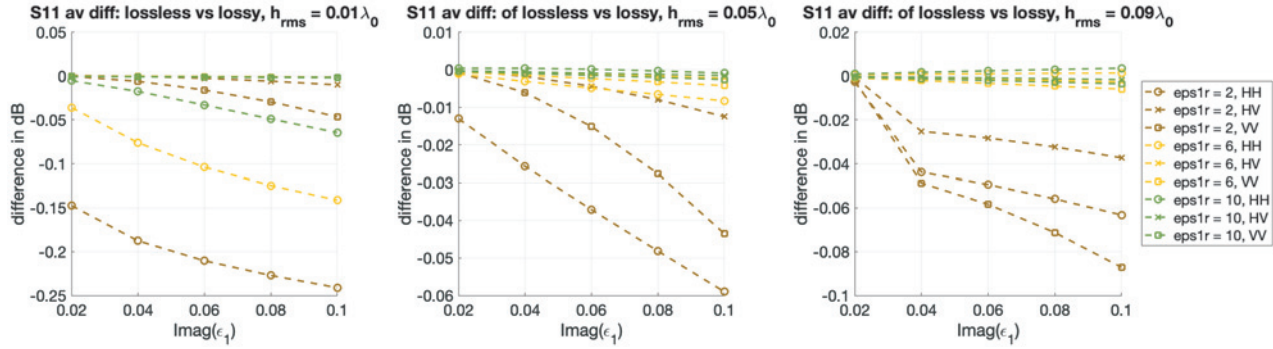


Figure 14. Averaged S_{11} difference between lossless and lossy cases.

derived from the Maxwell's Equations, such rapid solutions with acceptable error are useful trade-off in many applications, e.g., simulating microwave scattering from large-scale surfaces with facets. On the other hand, compared to direct lookup in the original datacube, having the datacube parametrized as analytical functions of the key variables allows 1) even faster pattern computation; 2) more accurate and immediate interpolation and extrapolation to predict patterns for cases not in the original simulation forming the datacube; 3) largely reduced data required to store in memory for computation, e.g., size of the original datacube in this work is 35.5 GB, while all the coefficients and lookup tables of the parametrization-based model take up only 15.8 MB storage space, which enables and is highly preferred in parallel computation, where only a small amount of data needs to be distributed and stored in the node cache memories.

4. CONCLUSION

A datacube parametrization-based model has been presented in this work for fast estimation of polarimetric bistatic scattering from a rough interface with different dielectric contrast. The model can be used to reconstruct the two-dimensional bistatic scattering patterns as a function of the surface roughness, the surface dielectric contrast, and the incident angle. Good agreement has been demonstrated in the reconstructed bistatic scattering pattern compared to the original ones from the input datacube. Though not physics-based, the datacube parametrization-based model allows quick estimation and reconstruction of the polarimetric bistatic scattering coefficients and patterns. The model development approach can also be adapted to parametrize datacubes from simulations with other configurations or targets, e.g., surface with different correlation functions, etc. Future work includes expansion of the model to bistatic scattering from high to low dielectric media, as well as to the estimation of the transmission coefficients.

ACKNOWLEDGMENT

The research was carried out at the Jet Propulsion Laboratory, California Institute of Technology, under a contract with the National Aeronautics and Space Administration (80NM0018D0004).

REFERENCES

1. Franceschetti, G., M. Migliaccio, D. Riccio, and G. Schirinzi, "Saras: A Synthetic Aperture Radar (SAR) raw signal simulator," *IEEE Transactions on Geoscience and Remote Sensing*, Vol. 30, No. 1, 110–123, 1992.
2. Nouvel, J.-F., A. Herique, W. Kofman, and A. Safaenili, "Radar signal simulation: Surface modeling with the facet method," *Radio Science*, Vol. 39, No. 1, 1–17, 2004.
3. Gerekos, C., A. Tamponi, L. Carrer, D. Castelletti, M. Santoni, and L. Bruzzone, "A coherent

- multilayer simulator of radargrams acquired by radar sounder instruments,” *IEEE Transactions on Geoscience and Remote Sensing*, Vol. 56, No. 12, 7388–7404, 2018.
4. Alessi, S., F. De Acutis, G. Picardi, and R. Seu, “Surface bistatic scattering coefficient by means the facet model radar altimetry application,” *1996 26th European Microwave Conference*, Vol. 1, 337–340, IEEE, 1996.
 5. Zhang, M., H. Chen, and H.-C. Yin, “Facet-based investigation on EM scattering from electrically large sea surface with two-scale profiles: Theoretical model,” *IEEE Transactions on Geoscience and Remote Sensing*, Vol. 49, No. 6, 1967–1975, 2011.
 6. West, J. C., R. K. Moore, and J. C. Holtzman, “The slightly-rough facet model in radar imaging of the ocean surface,” *International Journal of Remote Sensing*, Vol. 11, No. 4, 617–637, 1990.
 7. Garcia-Fernandez, A. F., O. A. Yeste-Ojeda, and J. Grajal, “Facet model of moving targets for ISAR imaging and radar back-scattering simulation,” *IEEE Transactions on Aerospace and Electronic Systems*, Vol. 46, No. 3, 1455–1467, 2010.
 8. Williams, K. L. and D. R. Jackson, “Bistatic bottom scattering: Model, experiments, and model/data comparison,” *The Journal of the Acoustical Society of America*, Vol. 103, No. 1, 169–181, 1998.
 9. Dahl, P. H., “On bistatic sea surface scattering: Field measurements and modeling,” *The Journal of the Acoustical Society of America*, Vol. 105, No. 4, 2155–2169, 1999.
 10. Fung, A. K., C. Zuffada, and C.-Y. Hsieh, “Incoherent bistatic scattering from the sea surface at L-band,” *IEEE Transactions on Geoscience and Remote Sensing*, Vol. 39, No. 5, 1006–1012, 2001.
 11. Khenchaf, A., “Bistatic scattering and depolarization by randomly rough surfaces: Application to the natural rough surfaces in X-band,” *Waves in Random Media*, Vol. 11, No. 2, 61–90, 2001.
 12. Tabatabaenejad, A. and M. Moghaddam, “Bistatic scattering from three-dimensional layered rough surfaces,” *IEEE Transactions on Geoscience and Remote Sensing*, Vol. 44, No. 8, 2102–2114, 2006.
 13. Johnson, J. T. and J. D. Ouellette, “Polarization features in bistatic scattering from rough surfaces,” *IEEE Transactions on Geoscience and Remote Sensing*, Vol. 52, No. 3, 1616–1626, 2013.
 14. Voronovich, A., “Small-slope approximation for electromagnetic wave scattering at a rough interface of two dielectric half-spaces,” *Waves in Random Media*, Vol. 4, No. 3, 337–368, 1994.
 15. Chou, H.-T. and J. T. Johnson, “A novel acceleration algorithm for the computation of scattering from rough surfaces with the forward-backward method,” *Radio Science*, Vol. 33, No. 5, 1277–1287, 1998.
 16. Kapp, D. A. and G. S. Brown, “A new numerical method for rough-surface scattering calculations,” *IEEE Transactions on Antennas and Propagation*, Vol. 44, No. 5, 711, 1996.
 17. Jandhyala, V., E. Michielssen, S. Balasubramaniam, and W. C. Chew, “A combined steepest descent-fast multipole algorithm for the fast analysis of three-dimensional scattering by rough surfaces,” *IEEE Transactions on Geoscience and Remote Sensing*, Vol. 36, No. 3, 738–748, 1998.
 18. Fung, A., W. Liu, K. Chen, and M. Tsay, “An improved iem model for bistatic scattering from rough surfaces,” *Journal of Electromagnetic Waves and Applications*, Vol. 16, No. 5, 689–702, 2002.
 19. Wu, T.-D., K.-S. Chen, J. Shi, H.-W. Lee, and A. K. Fung, “A study of an AIEM model for bistatic scattering from randomly rough surfaces,” *IEEE Transactions on Geoscience and Remote Sensing*, Vol. 46, No. 9, 2584–2598, 2008.
 20. Duan, X. and M. Moghaddam, “3-D vector electromagnetic scattering from arbitrary random rough surfaces using stabilized extended boundary condition method for remote sensing of soil moisture,” *IEEE Transactions on Geoscience and Remote Sensing*, Vol. 50, No. 1, 87–103, 2011.
 21. Zribi, M., N. Baghdadi, N. Holah, O. Fafin, and C. Guérin, “Evaluation of a rough soil surface description with asar-envisat radar data,” *Remote Sensing of Environment*, Vol. 95, No. 1, 67–76, 2005.
 22. Duan, X. and M. Haynes, “Supporting data for the datacube parametrization-based model for rough surface polarimetric bistatic scattering,” 2020, [Online], available: <http://dx.doi.org/10.21227/hg2q-b864>.